

Seismic Test of Solar Models, Solar Neutrinos and Implications for Metal-Rich Accretion

R. A. Winnick, Pierre Demarque and Sarbani Basu

Department of Astronomy, Yale University, Box 208101, New Haven, CT 06520-8101

and

D. B. Guenther

*Department of Astronomy and Physics, Saint Mary's University, Halifax, NS, Canada,
B3H 3C3*

ABSTRACT

The Sun is believed to have been the recipient of a substantial amount of metal-rich material over the course of its evolution, particularly in the early stages of the Solar System. With a long diffusion timescale, the majority of this accreted matter should still exist in the solar convection zone, enhancing its observed surface abundance, and implying a lower-abundance core. While helioseismology rules out solar models with near-zero metallicity cores, some solar models with enhanced metallicity in the convection zone might be viable, as small perturbations to the standard model. Because of the reduced interior opacity and core temperature, the neutrino flux predicted for such models is lower than that predicted by the standard solar model. This paper examines how compatible inhomogeneous solar models of this kind are with the observed low- l p -mode oscillation data, and with the solar neutrino data from the SNO Collaboration. We set an upper limit on how much metal-rich accretion took place during the early evolution of the Sun at $\sim 2M_{\oplus}$ of iron (or $\sim 40M_{\oplus}$ of meteoric material).

Subject headings: Sun: accretion, evolution, interior, oscillations, neutrinos

1. Introduction

Early on in the evolution of the Sun, the interstellar medium and young Solar System provided an environment capable of frequent accretion events. Material in the form of ISM,

proto-planets, planetesimals, comets, and asteroids frequently bombarded the Solar surface and were accreted. This accreted matter is deficient in hydrogen and helium, introducing metal-rich material into the upper layers of the Sun. Exactly how much metal-rich matter was accreted in these early stages and for how long, has been speculated by several authors (Christensen-Dalsgaard, Gough, & Morgan 1979, Jeffery et al. 1997), but unfortunately is not well known.

More recently, Murray et al. (2001) have searched a sample of 640 solar-type stars for the signature of iron enhancement in their spectra and concluded that, on average, these stars appear to have accreted about $0.5M_{\oplus}$ of iron while on the main sequence. They raise the possibility that the Sun may have accreted a similar amount of iron during its evolution. Whether helioseismology can detect this amount of accretion is uncertain. So far only one study has been published on the effect of accretion on the p -mode frequency (Henney & Ulrich 1998). These authors concluded that the accretion of $8M_{\oplus}$ of meteoric material (approximately $0.4M_{\oplus}$ of iron) on the Sun could not be detected by seismology due to other uncertainties in the models.

The main consequence of such accretion is the metal enrichment of the Sun’s surface and convection zone, while maintaining a lower-abundance core. In such a scenario, the expected neutrino flux is reduced due to the lower opacity and temperature in the central region of the Sun. It has long been known that solar models with near-zero metallicity cores can lower the predicted neutrino flux, and this explanation was discussed early-on as a possible solution of the classical neutrino problem (see e.g. the review by Rood 1978). More recently, Guenther & Demarque (1997, hereafter GD97) have constructed solar models with low- Z cores using present physics and found their p -mode frequencies to be incompatible with solar p -mode observations.

This paper describes work which can be viewed as an extension of GD97; but this time we examine the limits set by helioseismology on the non-standard assumption that the solar convection zone of the Sun has been enriched in heavy elements by accretion during its early evolution. In addition to comparing the p -mode frequencies to observation in the frequency difference diagram, as done by GD97, we also compare the calculated sound-speed and density in our models to the same quantities derived from observation by inversion (Basu & Antia 1997, hereafter BA97; Basu, Pinsonneault & Bahcall 2000, hereafter BPB00).

Since this research was begun, the first results from the Sudbury Neutrino Observatory (SNO) experiment have been released (Ahmad et al. 2001). Ahmad et al. (2001) conclude that the ^8B neutrino flux derived from their observations, i.e. $\Phi_{s_B} = 5.44 \pm 0.99 \times 10^6 \text{ cm}^{-2}\text{s}^{-1}$, agrees with the predictions of the best standard solar models. Any accretion model must then also be constrained by the SNO observations, in addition to the constraints of

helioseismology.

2. Assumptions and Method

The main assumption in this paper is that the accretion of heavy elements onto the Sun took place during the early evolution of the Sun, at a time when the Sun was near the main sequence, i.e. when the convection zone had reached its main sequence value. The convection is shallow at this time, and only the outer 2% of the Sun’s mass in the convection zone get enriched.

As in GD97, the solar models were constructed using the Yale stellar evolution code (YREC for Yale Rotating Evolution Code) in its non-rotating configuration (Guenther et al. 1992). The energy generation routines used in YREC are those of Bahcall & Pinsonneault (1992). The cross sections are as listed in Bahcall (1989), with updates from GD97. The equation of state tables prepared by the OPAL researchers (Rogers 1986, Rogers, Swenson, & Iglesias 1996) were used for the models. OPAL opacity tables (Iglesias & Rogers 1996) were used to derive interior opacities, while Alexander & Ferguson (1994) low temperature opacity tables were used to derive surface and atmosphere opacities.

All models were evolved from a zero-age main sequence (ZAMS) model to near the age of the Sun in 50 equally spaced time steps. The age of the Sun was taken to be 4.5 Gyr, close to the meteoric solar age (Guenther 1989). As was noted by GD97, standard solar models of this age are in best agreement with the calculated oscillation spectra. The mixing length/pressure scale height ratio, α , was assumed to be 1.9, producing a standard solar model (Guenther et al. 1992). Most models were tuned to match the observed solar radius to one part in 10^7 ($R_{\odot}=6.958 \times 10^{10}$ cm) and the solar luminosity to one part in 10^6 ($L_{\odot}=3.8515 \times 10^{33}$ ergs s $^{-1}$). Models #4, 8, and 18 (see Table 1) did not converge at the aforementioned tolerance for radius, but converged to the solar radius to one part in 10^6 . Model #20 required an even lower tolerance, matching the solar radius to one part in 10^5 . The number of shells in standard solar models #17 and 18 was 1892, and 1893 in models #19 and 20. There were more than 2300 shells in all non-standard solar models. Tests have shown that at least that many shells are needed to obtain the required precision in the calculation of the p -mode frequencies (Guenther et al. 1992; Guenther 1994).

Helium and heavy element diffusion were included in all of the solar models due to their necessary role in finding simultaneous agreement with both the observed value of $(Z/X)_{\odot}$ and the p -mode spectrum (for further details see GD97). The assumption made regarding the nonstandard models is that the Sun’s interior, (defined here as $R < R_{\text{env}}$), is composed of

material at a lower heavy-element abundance than the Sun’s surface due to the accretion of metal-rich matter. In order to produce such nonstandard solar models with low- Z interiors, the run of Z in the initial ZAMS model was modified. The interior metal abundance was initially set to the homogeneous value of Z_{int} out to $(M/M_{\odot})=0.9$, indicating a metal-poor interior. The more metal-rich exterior of the Sun, $(M/M_{\odot})\geq 0.975$, was setup with a metal abundance of Z_{init} . Z_{int} and Z_{init} represent ZAMS mass fractions of all heavy elements for the interior and exterior, respectively. In the intermediate region, $0.9\leq(M/M_{\odot})\leq 0.975$, Z linearly increases from Z_{int} to Z_{init} .

In deciding what value Z_{int} might be for the nonstandard solar models, it is relevant to note that the Sun is observed to be more metal rich than the surrounding ISM, with Z_{ISM} possibly as low as 65% of Z_{\odot} (Mathis 1996). Believing the Sun formed from material typical of the ISM, the metal-enhanced exterior could have resulted from the bombardment of metal-rich material in the form of comets, asteroids, planetesimals and proto-planets. With a long diffusion timescale, most of this material should still exist in the upper layers of the Sun, leaving the interior metal-poor, much like the surrounding ISM. With this in mind, we chose a value of $Z_{\text{int}}=0.65Z_{\odot}$. Other values of $0.30Z_{\odot}$, $0.50Z_{\odot}$, and $0.80Z_{\odot}$ were also examined.

A choice of $Z_{\text{int}} = 0.80Z_{\text{init}}$ corresponds to an accretion enhancement of about $2M_{\oplus}$ in iron, or about $40M_{\oplus}$ in meteoric material. Similarly, $Z_{\text{int}}=0.65Z_{\text{init}}$, $Z_{\text{int}}=0.50Z_{\text{init}}$, and $Z_{\text{int}}=0.30Z_{\text{init}}$ corresponds to about $2.9M_{\oplus}$, $4.1M_{\oplus}$ and $5.7M_{\oplus}$, respectively, in iron accretion, or about $60M_{\oplus}$, $80M_{\oplus}$ and $120M_{\oplus}$, respectively, in meteoric material accretion.

Four standard solar models were created, differing only by the value of Z_{init} , the initial or ZAMS mass fraction value of all heavy elements in the solar exterior. Without the assumption of a more metal-poor interior, Z_{int} is assumed equivalent to Z_{init} . Values of Z_{init} were taken as 0.0170, 0.0188, 0.0200, and 0.0220. These standard solar models comprise models #17-20 in Tables 1-3. Z_{init} was also varied in the nonstandard solar models, thus along with the varying Z_{int} , a grid was created, comprising models #1-16 in Tables 1-3.

Physical characteristics of both the standard (#17-20) and nonstandard (#1-16) solar models are listed in Table 1. Table 1 includes, from left to right: Model, the model number; Type, the type of model, where NSSM stands for a nonstandard solar model and SSM stands for a standard solar model; X_{init} , the initial or ZAMS mass fraction value of hydrogen; Z_{init} , the initial or ZAMS mass fraction value of all heavy elements in the solar exterior; $Z_{\text{int}}/Z_{\text{init}}$, the initial or ZAMS mass fraction value of all heavy elements in the solar interior relative to Z_{init} ; X_{surf} , the surface mass fraction value of hydrogen at the evolved age; Z_{surf} , the surface mass fraction of all heavy elements at the evolved age; M_{env} , the fraction of the total mass contained in the outer convective envelope; R_{env} , the radius fraction of the base of

the convective envelope; $\log P_c$, the base ten logarithm of the central pressure; $\log T_c$, the base ten logarithm of the central temperature; $\log \rho_c$, the base ten logarithm of the central density; X_c , the central mass fraction of heavy elements; Z_c , the central mass fraction of heavy elements.

The nuclear energy generation properties of both the standard (#17-20) and nonstandard (#1-16) solar models are listed in Table 2. Table 2 lists the fraction of total photon luminosity coming from the PP I, PP II, and PP III branches of the PP network and from the CNO cycle. Also listed are the individual neutrino fluxes from the neutrino producing reactions that occur in the sun (see Figure 1 of GD97). Note that in GD97 the neutrino fluxes are listed in units of $10^{10}\text{cm}^{-2}\text{s}^{-1}$. Finally, Table 2 lists $\Phi(^{37}\text{Cl})$, the total neutrino flux, in SNU, for the ^{37}Cl detector; and $\Phi(^{71}\text{Ga})$, the total neutrino flux, in SNU, for the ^{71}Ga detector.

3. p -mode Frequencies

As a test on the validity of a model, the expected oscillation frequencies can be compared with observations from the Sun. Guenther’s non-radial, non-adiabatic pulsation program (Guenther 1994) was used to calculate the oscillation frequencies of the models produced with YREC. The model output was then compared with data obtained by the Michelson Doppler Imager (MDI) instrument on board the *Solar and Heliospheric Observatory (SOHO)* during the first year of its operation (Rhodes et al. 1997).

From these data, p -mode frequency differences: $\nu_{\text{model}} - \nu_{\odot}$, were computed for $l=0-4, 10, 20, 30, 40, 50, 60, 70, 80, 90,$ and 100 . Frequency difference plots (model frequency minus observed frequency versus observed frequency) were then constructed for each model and can be seen in Figure 1. Each line joins together data of a common l -value, hence joining together p -modes with approximately similar inner turning points. In the event of perfect seismic agreement with the Sun, a frequency difference plot would show a straight horizontal line at $0 \mu\text{Hz}$, indicating that the p -mode frequency differences were zero. Instead, Figure 1 shows a more complex bundle of lines, indicating discrepancies of our models from the Sun. As in GD97, the quality of a models’ agreement with the Sun is judged on the tightness of the bundle of lines. The underlying slope error present is thought to be due to modeling errors in the very outermost layers of the Sun, a region of known uncertainties. The errors in the interior of the model, primarily near the base of the convection zone, are directly correlated to the bundle thickness in the sense that the tighter the bundle, the better the model is at fitting the region near and above the convection zone. (See GD97 for further details.)

Figure 1 is a 4×5 grid of plots showing the frequency differences for each of the 20 models computed. Each plot is annotated by its model number (see Tables 1-3), the surface Z/X ratio, and ${}^8\text{B}$ neutrino flux, in $\text{cm}^{-2}\text{s}^{-1}$. Lines connect common l -values, with $l=0-4, 10, 20, 30, 40, 50, 60, 70, 80, 90,$ and 100 . As indicated by the model numbers, the four standard solar models computed in this work comprise the last row in Figure 1.

Special consideration was given to low- l p -modes due to their ability to probe the deep interior of the Sun. This is due to the fact that the inner turning points of these modes are located closest to the core. Low- l p -modes are still sensitive to the outer layers, but this effect can be canceled out by subtracting from a given p -mode frequency the frequency of a p -mode with a similar eigenfunction shape in the outer layers and distinct eigenfunction shape in the deeper layers. The small spacing difference, defined as $\delta\nu(n, l) = \nu(n, l) - \nu(n-1, l+2)$, thus provides a further diagnostic of the deep interior of the Sun. (See GD97 for further details.) To compare our models with observations from the Sun, small spacing differences plots were produced [i.e., $\delta\nu_{\text{model}}(n, l) - \delta\nu_{\odot}(n, l)$ vs. $\nu_{\odot}(n, l)$]. As in the case of the frequency difference plots, the closer $\delta\nu_{\text{model}}(n, l) - \delta\nu_{\odot}(n, l)$ is to $0 \mu\text{Hz}$, the better the agreement between the observations and a model.

Since the sensitivity of the small spacings to the deep interior of the Sun diminishes with increasing l , only those p -modes with $l=0, 1,$ and 2 were used to contrast the models with observed values from the Sun. The small spacing difference plots can be seen in Figure 2. Figure 2 is a 3×5 grid in which each row contains models of the same Z_{int} , where $Z_{\text{int}}=0.30Z_{\text{init}}$ includes models #1-4, $Z_{\text{int}}=0.50Z_{\text{init}}$ includes models #5-8, $Z_{\text{int}}=0.65Z_{\text{init}}$ includes models #9-12, $Z_{\text{int}}=0.80Z_{\text{init}}$ includes models #13-16, and $Z_{\text{int}}=Z_{\text{init}}$ includes the standard solar models #17-20. Each column in Figure 2 contains results for a common l -value, with $l=0$ in column 1, $l=1$ in column 2, and $l=2$ in column 3. Lines in each panel represent models with the same Z_{int} with differing Z_{init} values ranging from 0.0170 to 0.0220 , as indicated.

4. Sound-speed and Density

Figure 3 shows the relative sound-speed differences for the twenty models presented in this paper compared to the observed solar sound-speed, derived from an inversion of the solar p -mode frequencies (Christensen-Dalsgaard, Gough & Thompson 1991; BA97). We note the superior agreement of the standard solar models with observation, especially model #20, as compared to the non-standard models. Similarly, Figure 4 shows the same plots for density. The less precise agreement with densities than with sound-speed is in part a reflection of the greater uncertainty in density inversions.

5. Discussion of the Models

5.1. Choice of a Benchmark Standard Solar Model

Figure 1 shows the characteristics of the standard solar models (#17-20) in the frequency difference diagram. Best agreement with observation, as measured by the thickness of the line bundles corresponding to different l -values, favors #20 and 19. Note that our model #19 is nearly identical to model #20 of GD97, that was judged by GD97 as the “best” standard solar model in their study. But our model #20, which is intermediate in Z_{init} between GD97’s models #20 and 21, is a better model still. The bundle of l -values in model #20 is thinner than in model #19, a fact which is also reflected in the best agreement with observation in the sound-speed plot shown in Figure 3.

In selecting a “best” standard solar model, one should also take into account two additional constraints. The first constraint, to which we will assign the most weight, is the solar convection zone depth, R_{env} , which has been derived by sound-speed inversion (Christensen-Dalsgaard et al. 1991; BA97). The second additional constraint is Y_{surf} for the Sun. This quantity can also be estimated by inversion of the p -mode data (Basu 1998).

For model #20, we have $R_{\text{env}} = 0.7129$, to be compared to $R_{\text{env}} = 0.713 \pm 0.001$ from inversion (BA97). This agreement is confirmed by the sound-speed plot for model #20 (see Figures 3 and 6), which shows close agreement with the inversion data. At the same time, model #20 yields $Y_{\text{surf}} = 0.2519$, to be compared to the helium mass fraction 0.248 ± 0.003 derived by Basu (1998), a satisfactory agreement in view of the uncertainties in diffusion coefficients and efficiency. On the other hand, both the surface metallicity $(Z/X)_{\text{surf}}$ and the ^8B neutrino flux for model #20 are a little too large. But we see that a model interpolated between models #20 and 19 would satisfy all constraints within the errors.

As it is, model #20 is an excellent standard solar model, as illustrated in Figures 3-7. Comparing Figures 2 and 3 in BPB00 with our Figures 6 and 7, we see that model #20 compares favorably with model BP2000.

The small spacing plots (Figure 2) shows that all our standard models, models #17-20, agree equally well with observation. Within the range of chemical composition we have considered, small spacings are insensitive to the choice of initial heavy element content. Figure 5 shows the zoomed-in small spacing plot for $l=0$ for standard solar model #20. Error bars calculated from the MDI-SOHO data set used are also plotted. The observational uncertainties are approximately $\pm 0.07 \mu\text{Hz}$ for the small spacing determination. From this figure, the numerical uncertainties in the solar model appear to be approximately ± 0.05 to $0.10 \mu\text{Hz}$ for the small spacing calculation. The larger uncertainties of $\pm 1 \mu\text{Hz}$ for the mode

frequencies themselves cancel out somewhat when calculating the small spacings.

It is difficult to evaluate the uncertainty in the observed solar heavy element content $(Z/X)_{\text{surf}}$. GD97 used $(Z/X)_{\text{surf}} = 0.0244 \pm 0.001$, from Grevesse, Noels & Sauval (1996). More recent lower estimates suggest that large systematic errors may still exist in the measurements. Grevesse & Sauval (1998) find $(Z/X)_{\text{surf}} = 0.0230$, quoting a 10% error estimate. Asplund (2000), using a stellar model atmosphere constructed with a more realistic treatment of convection, derives $(Z/X)_{\text{surf}} = 0.0226$. Unfortunately, theoretical estimates for both Y_{surf} and $(Z/X)_{\text{surf}}$ are also difficult to make, due to the uncertainties in calculating the efficiency of diffusion just below the convection zone in the stellar interior (Chaboyer et al. 1995). Helioseismic sound-speed inversion shows that the tachocline structure is one of the least well-understood features of standard solar models (BA97).

Standard models #18-20 all have ${}^8\text{B}$ neutrino fluxes in agreement with the SNO data.

Table 3 summarizes the values of the constraints considered here for each solar model computed in this work. Listed are the Model, R_{env} , Y_{surf} , ${}^8\text{B}$ and $(Z/X)_{\text{surf}}$.

5.2. Non-Standard Solar Models

At first glance, the frequency difference diagram in Figure 1 does not reveal much difference in bundle thickness between the non-standard models #7, 8, 11, and 15 and the standard model #19. The l -value bundle for model #12 seems even slightly thinner. But models #7, 8, 11 and 12 are all readily ruled out by the ${}^8\text{B}$ neutrino constraint.

Non-standard model #16 is similar to standard model #20 in having the thinnest l -value bundles, and it satisfies the ${}^8\text{B}$ neutrino constraint. But it passes the $(Z/X)_{\text{surf}}$ test only marginally. Non-standard models #10 and 15, like standard model #20, pass the convection zone depth test, but of these, only #15 passes the $(Z/X)_{\text{surf}}$ test, and it fails the ${}^8\text{B}$ neutrino test by a small amount.

Turning to the small spacing diagram (Figure 2), we see that the non-standard models agree as well with observation as the standard models only for $l = 0$. But for $l = 1$ and $l = 2$, there is an increasing discrepancy with decreasing Z_{int} . The maximum discrepancy is only $2 \mu\text{Hz}$, however, which may still be within the uncertainties. As in the case of the standard models, heavy element content plays little role.

We conclude then that of all the non-standard solar models listed in Tables 1-3, only models #15 and 16 are marginally acceptable. We can use these two models to set an upper limit to the amount of heavy element accretion during the early main sequence evolution of

the Sun.

6. Summary and Conclusions

A set of standard solar models were first constructed using the same physics and stellar evolution code as GD97, to serve as benchmarks for our non-standard models. Although our purpose was not to achieve the best possible fit to observation, we find that our standard solar model #20 satisfies the most stringent constraints from helioseismology at least as well as the best published standard solar model. It is just outside the 1σ limit for the $(Z/X)_{\text{surf}}$ constraint and for the SNO Collaboration ^8B neutrino flux. It is apparent that a standard solar model in full agreement with all up-to-date observational data would be achieved with the same physics as in GD97, for a Z_{init} intermediate between model #19 and model #20, i.e. for $0.020 < Z_{\text{init}} < 0.022$. It would also be interesting to probe intermediate values of Z_{int} , with $0.80 < Z_{\text{int}} < 1.00$.

There has been interest during the past few years in the effects of accretion on the Sun during its evolution. With this application in mind, the main purpose of this paper was to study the properties of a number of non-standard solar models in which the convection zone is richer in heavy elements than the interior, and to explore the constraints of helioseismology on such models.

None of our non-standard solar models agree as well with observation as our best standard models. But two of the least extreme non-standard solar models, models #15 and 16, come close to satisfying all of the observational constraints. For this reason, they provide a realistic upper limit of $\sim 2M_{\oplus}$ of iron (or $\sim 40M_{\oplus}$ of meteoric material) to the accretion experienced by the Sun during its early main sequence phase. This conclusion is compatible with Henney & Ulrich's (1998) earlier null result that the accretion of $8M_{\oplus}$ of meteoric material on the Sun could not at this point be detected by seismology because of the uncertainties. Similarly, a solar enrichment of $0.5M_{\oplus}$ in iron, as suggested recently by Murray et al. (2001), is beyond detectability by seismic means at the present time.

This work was supported in parts by NASA grant NAG5-8406 (PD), a grant from NSERC Canada (DBG), and NASA grant NAG5-10912 (SB). This work utilizes data obtained by the Solar Oscillations Investigation / Michelson Doppler Imager on the Solar and Heliospheric Observatory (SOHO). SOHO is a project of international cooperation between ESA and NASA. MDI is supported by NASA grants NAG5-8878 and NAG5-10483 to Stanford University.

REFERENCES

- Ahmad et al. 2001, *Phys. Rev. Lett.*, 87, 071301
- Asplund, M. 2000, *A&A*, 359, 755
- Alexander, D. R., & Ferguson, J. W. 1994, *ApJ*, 437, 879
- Bahcall, J. N. 1989, *Neutrino Astrophysics* (Cambridge: Cambridge Univ. Press)
- Bahcall, J. N., & Pinsonneault, M. H. 1992, *Rev. Mod. Phys.*, 60, 297
- Basu, S. 1998, *MNRAS*, 298, 719
- Basu, S. & Antia, H.M. 1997, *MNRAS*, 287, 189 (BA97)
- Basu, S., Pinsonneault, M.H., & Bahcall, J.N. 2000, *ApJ*, 529, 1084 (BPB00)
- Chaboyer, B., Demarque, P., Guenther, D.B., & Pinsonneault, M.H. 1995, *ApJ*, 446, 435
- Christensen-Dalsgaard, J., Gough, D.O., & Morgan, J.G. 1979, *A&A*, 73, 121
- Christensen-Dalsgaard, J., Gough, D.O., & Thompson, M.J. 1991, *ApJ*, 378, 413
- Grevesse, N., Noels, A. & Sauval, A.J. 1996, in *ASP Conf. Ser.99, Cosmic Abundances*, ed. S.S. Holt & G. Sonneborn (San Francisco:ASP), 117
- Grevesse, N., & Sauval, A.J. 1998, *Space Sci. Rev.*, 85, 161
- Guenther, D.B. 1989, *ApJ*, 339, 1156
- Guenther, D.B. 1994, *ApJ*, 422, 400
- Guenther, D. B., Demarque, P., Kim, Y.-C., & Pinsonneault, M. H. 1992, *ApJ*, 387, 372
- Guenther, D. B. & Demarque, P. 1997, *ApJ*, 484, 937 (GD97)
- Henney, C.J., & Ulrich, R.K. 1998, in *Structure and Dynamics of the Interior of the Sun and Sun-like Stars*, ed. S. Korzennik & A. Wilson (Noordwijk:ESA), 473
- Iglesias, C. A., & Rogers, F. J. 1996, *ApJ*, 464, 943
- Jeffery, C. S., Bailey, M. E. & Chambers, J. E. 1997, *The Observatory*, 117, 224
- Mathis, J. S. 1996, *ApJ*, 472, 643
- Murray, N., Chaboyer, B., Arras, P., Hansen, B., & Noyes, R.W. 2001, *ApJ*, 555, 801
- Rhodes, E.J. Jr., Kosovichev, A.G., Schou, J., Scherrer, P.H., & Reiter, J. 1997, *Sol. Phys.*, 175, 287
- Rogers, F. J. 1986, *ApJ*, 310, 723
- Rogers, F. J., Swenson, F. J., & Iglesias, C. A. 1996, *ApJ*, 456, 902

Rood, R.T. 1978, in Proc. Informal Conf. Status and Future of Solar Neutrino Research,
ed. G. Friedlander, BNL-50879, 1, 175

Table 1. Solar Model Characteristics

| Model | Type | X_{init} | Z_{init} | $Z_{\text{int}}/Z_{\text{init}}$ | X_{surf} | Z_{surf} | M_{env} | R_{env} | $\log P_c$ | $\log T_c$ | $\log \rho_c$ | X_c | Z_c |
|-------|------|-------------------|-------------------|----------------------------------|-------------------|-------------------|------------------|------------------|------------|------------|---------------|-------|--------|
| 1 | NSSM | 0.8145 | 0.0170 | 0.30 | 0.8359 | 0.0153 | 0.02021 | 0.7133 | 17.354 | 7.160 | 2.148 | 0.467 | 0.0053 |
| 2 | NSSM | 0.8066 | 0.0188 | 0.30 | 0.8281 | 0.0170 | 0.02203 | 0.7070 | 17.356 | 7.162 | 2.151 | 0.460 | 0.0059 |
| 3 | NSSM | 0.8013 | 0.0200 | 0.30 | 0.8230 | 0.0181 | 0.02335 | 0.7025 | 17.357 | 7.163 | 2.153 | 0.455 | 0.0063 |
| 4 | NSSM | 0.7929 | 0.0220 | 0.30 | 0.8151 | 0.0199 | 0.02475 | 0.6982 | 17.358 | 7.165 | 2.155 | 0.447 | 0.0069 |
| 5 | NSSM | 0.7813 | 0.0170 | 0.50 | 0.8063 | 0.0153 | 0.02065 | 0.7164 | 17.361 | 7.170 | 2.160 | 0.430 | 0.0089 |
| 6 | NSSM | 0.7702 | 0.0188 | 0.50 | 0.7955 | 0.0169 | 0.02274 | 0.7096 | 17.364 | 7.173 | 2.165 | 0.419 | 0.0099 |
| 7 | NSSM | 0.7629 | 0.0200 | 0.50 | 0.7884 | 0.0180 | 0.02409 | 0.7057 | 17.365 | 7.175 | 2.168 | 0.412 | 0.0105 |
| 8 | NSSM | 0.7545 | 0.0220 | 0.50 | 0.7805 | 0.0198 | 0.02522 | 0.7026 | 17.366 | 7.178 | 2.170 | 0.404 | 0.0115 |
| 9 | NSSM | 0.7608 | 0.0170 | 0.65 | 0.7880 | 0.0153 | 0.02083 | 0.7185 | 17.365 | 7.177 | 2.168 | 0.407 | 0.0116 |
| 10 | NSSM | 0.7517 | 0.0188 | 0.65 | 0.7790 | 0.0169 | 0.02264 | 0.7124 | 17.367 | 7.180 | 2.171 | 0.398 | 0.0128 |
| 11 | NSSM | 0.7454 | 0.0200 | 0.65 | 0.7729 | 0.0180 | 0.02367 | 0.7095 | 17.368 | 7.181 | 2.173 | 0.392 | 0.0137 |
| 12 | NSSM | 0.7355 | 0.0220 | 0.65 | 0.7635 | 0.0198 | 0.02496 | 0.7058 | 17.369 | 7.184 | 2.176 | 0.383 | 0.0150 |
| 13 | NSSM | 0.7461 | 0.0170 | 0.80 | 0.7750 | 0.0153 | 0.02060 | 0.7211 | 17.368 | 7.182 | 2.172 | 0.391 | 0.0143 |
| 14 | NSSM | 0.7356 | 0.0188 | 0.80 | 0.7649 | 0.0169 | 0.02218 | 0.7163 | 17.370 | 7.185 | 2.176 | 0.380 | 0.0158 |
| 15 | NSSM | 0.7283 | 0.0200 | 0.80 | 0.7578 | 0.0180 | 0.02346 | 0.7122 | 17.371 | 7.188 | 2.178 | 0.373 | 0.0168 |
| 16 | NSSM | 0.7169 | 0.0220 | 0.80 | 0.7470 | 0.0198 | 0.02482 | 0.7085 | 17.373 | 7.191 | 2.182 | 0.362 | 0.0185 |
| 17 | SSM | 0.7264 | 0.0170 | 1.00 | 0.7576 | 0.0152 | 0.02043 | 0.7244 | 17.369 | 7.190 | 2.178 | 0.363 | 0.0179 |
| 18 | SSM | 0.7139 | 0.0188 | 1.00 | 0.7455 | 0.0169 | 0.02212 | 0.7195 | 17.371 | 7.194 | 2.182 | 0.348 | 0.0198 |
| 19 | SSM | 0.7057 | 0.0200 | 1.00 | 0.7375 | 0.0180 | 0.02336 | 0.7159 | 17.372 | 7.197 | 2.185 | 0.339 | 0.0210 |
| 20 | SSM | 0.6960 | 0.0220 | 1.00 | 0.7283 | 0.0198 | 0.02449 | 0.7129 | 17.372 | 7.201 | 2.188 | 0.326 | 0.0232 |

Table 2. Solar Model Nuclear Data^a

| Model# | Fraction of Total Luminosity | | | | Solar Neutrino Flux ^b | | | | | | | | | |
|--------|------------------------------|--------|--------|--------|----------------------------------|--------------------------|--------------------------|--------------------------------------|-------------------------------------|--------------------------------------|--------------------------------------|--------------------------------------|------------------------|------------------------|
| | PPI | PPII | PPIII | CNO | PP ($\times 10^{10}$) | PeP ($\times 10^8$) | HeP ($\times 10^3$) | ⁷ Be ($\times 10^9$) | ⁸ B ($\times 10^6$) | ¹³ N ($\times 10^8$) | ¹⁵ O ($\times 10^8$) | ¹⁷ F ($\times 10^6$) | $\Phi(^{37}\text{Cl})$ | $\Phi(^{71}\text{Ga})$ |
| 1 | 0.9471 | 0.0468 | 0.0039 | 0.0025 | 6.31 | 1.62 | 1.56 | 2.12 | 1.05 | 1.11 | 0.68 | 0.73 | 1.99 | 97.5 |
| 2 | 0.9441 | 0.0492 | 0.0041 | 0.0030 | 6.29 | 1.61 | 1.54 | 2.22 | 1.16 | 1.29 | 0.81 | 0.88 | 2.13 | 98.6 |
| 3 | 0.9420 | 0.0508 | 0.0043 | 0.0033 | 6.29 | 1.60 | 1.53 | 2.30 | 1.23 | 1.42 | 0.90 | 0.99 | 2.24 | 99.4 |
| 4 | 0.9386 | 0.0534 | 0.0045 | 0.0039 | 6.27 | 1.60 | 1.51 | 2.42 | 1.36 | 1.64 | 1.07 | 1.18 | 2.42 | 101 |
| 5 | 0.9317 | 0.0610 | 0.0051 | 0.0025 | 6.24 | 1.56 | 1.46 | 2.76 | 1.77 | 1.05 | 0.73 | 0.82 | 2.91 | 103 |
| 6 | 0.9261 | 0.0656 | 0.0055 | 0.0031 | 6.22 | 1.55 | 1.43 | 2.97 | 2.04 | 1.26 | 0.91 | 1.03 | 3.28 | 105 |
| 7 | 0.9222 | 0.0689 | 0.0058 | 0.0036 | 6.20 | 1.54 | 1.42 | 3.12 | 2.25 | 1.42 | 1.05 | 1.20 | 3.55 | 107 |
| 8 | 0.9175 | 0.0725 | 0.0061 | 0.0042 | 6.18 | 1.53 | 1.40 | 3.29 | 2.50 | 1.68 | 1.26 | 1.45 | 3.88 | 109 |
| 9 | 0.9203 | 0.0718 | 0.0060 | 0.0023 | 6.20 | 1.53 | 1.40 | 3.25 | 2.46 | 0.90 | 0.67 | 0.77 | 3.77 | 108 |
| 10 | 0.9149 | 0.0763 | 0.0064 | 0.0027 | 6.17 | 1.51 | 1.38 | 3.46 | 2.79 | 1.08 | 0.83 | 0.96 | 4.19 | 110 |
| 11 | 0.9111 | 0.0795 | 0.0067 | 0.0031 | 6.16 | 1.50 | 1.36 | 3.60 | 3.04 | 1.21 | 0.94 | 1.10 | 4.51 | 112 |
| 12 | 0.9047 | 0.0848 | 0.0071 | 0.0038 | 6.13 | 1.49 | 1.34 | 3.85 | 3.47 | 1.46 | 1.16 | 1.36 | 5.05 | 114 |
| 13 | 0.9109 | 0.0811 | 0.0068 | 0.0016 | 6.16 | 1.50 | 1.35 | 3.68 | 3.17 | 0.60 | 0.47 | 0.55 | 4.62 | 111 |
| 14 | 0.9040 | 0.0871 | 0.0073 | 0.0019 | 6.13 | 1.48 | 1.33 | 3.95 | 3.67 | 0.75 | 0.60 | 0.71 | 5.25 | 115 |
| 15 | 0.8990 | 0.0914 | 0.0077 | 0.0022 | 6.11 | 1.47 | 1.31 | 4.15 | 4.07 | 0.85 | 0.69 | 0.82 | 5.73 | 117 |
| 16 | 0.8907 | 0.0986 | 0.0083 | 0.0028 | 6.07 | 1.45 | 1.28 | 4.48 | 4.77 | 1.04 | 0.88 | 1.05 | 6.59 | 121 |
| 17 | 0.8877 | 0.0947 | 0.0080 | 0.0101 | 6.04 | 1.45 | 1.28 | 4.30 | 4.41 | 3.81 | 3.17 | 3.78 | 6.36 | 123 |
| 18 | 0.8758 | 0.1030 | 0.0087 | 0.0129 | 5.99 | 1.42 | 1.24 | 4.68 | 5.29 | 4.83 | 4.12 | 4.96 | 7.49 | 129 |
| 19 | 0.8672 | 0.1088 | 0.0092 | 0.0152 | 5.95 | 1.40 | 1.22 | 4.95 | 5.96 | 5.64 | 4.89 | 5.92 | 8.35 | 133 |
| 20 | 0.8559 | 0.1159 | 0.0098 | 0.0189 | 5.89 | 1.37 | 1.19 | 5.27 | 6.87 | 6.95 | 6.13 | 7.48 | 9.52 | 139 |

^a1-16 Non-Standard Solar Models, 17-20 Standard Solar Models^bValues given in units of $\text{cm}^{-2}\text{s}^{-1}$, except $\Phi(^{37}\text{Cl})$ and $\Phi(^{71}\text{Ga})$, which are given in SNU.

Table 3. Solar Model Constraint Values^a

| Model | R_{env} | Y_{surf} | ${}^8\text{B}$ | $(Z/X)_{\text{surf}}$ |
|-------|------------------|-------------------|----------------|-----------------------|
| 1 | 0.7133 | 0.1488 | 1.05 | 0.0183 |
| 2 | 0.7070 | 0.1549 | 1.16 | 0.0205 |
| 3 | 0.7025 | 0.1589 | 1.23 | 0.0220 |
| 4 | 0.6982 | 0.1650 | 1.36 | 0.0244 |
| 5 | 0.7164 | 0.1784 | 1.77 | 0.0190 |
| 6 | 0.7096 | 0.1876 | 2.04 | 0.0212 |
| 7 | 0.7057 | 0.1936 | 2.25 | 0.0228 |
| 8 | 0.7026 | 0.1997 | 2.50 | 0.0254 |
| 9 | 0.7185 | 0.1967 | 2.46 | 0.0194 |
| 10 | 0.7124 | 0.2041 | 2.79 | 0.0217 |
| 11 | 0.7095 | 0.2091 | 3.04 | 0.0233 |
| 12 | 0.7058 | 0.2167 | 3.47 | 0.0259 |
| 13 | 0.7211 | 0.2097 | 3.17 | 0.0197 |
| 14 | 0.7163 | 0.2182 | 3.67 | 0.0221 |
| 15 | 0.7122 | 0.2242 | 4.07 | 0.0238 |
| 16 | 0.7085 | 0.2332 | 4.77 | 0.0265 |
| 17 | 0.7244 | 0.2272 | 4.41 | 0.0201 |
| 18 | 0.7195 | 0.2376 | 5.29 | 0.0227 |
| 19 | 0.7159 | 0.2445 | 5.96 | 0.0244 |
| 20 | 0.7129 | 0.2519 | 6.87 | 0.0272 |

^a1-16 Non-Standard Solar Models, 17-20 Standard Solar Models

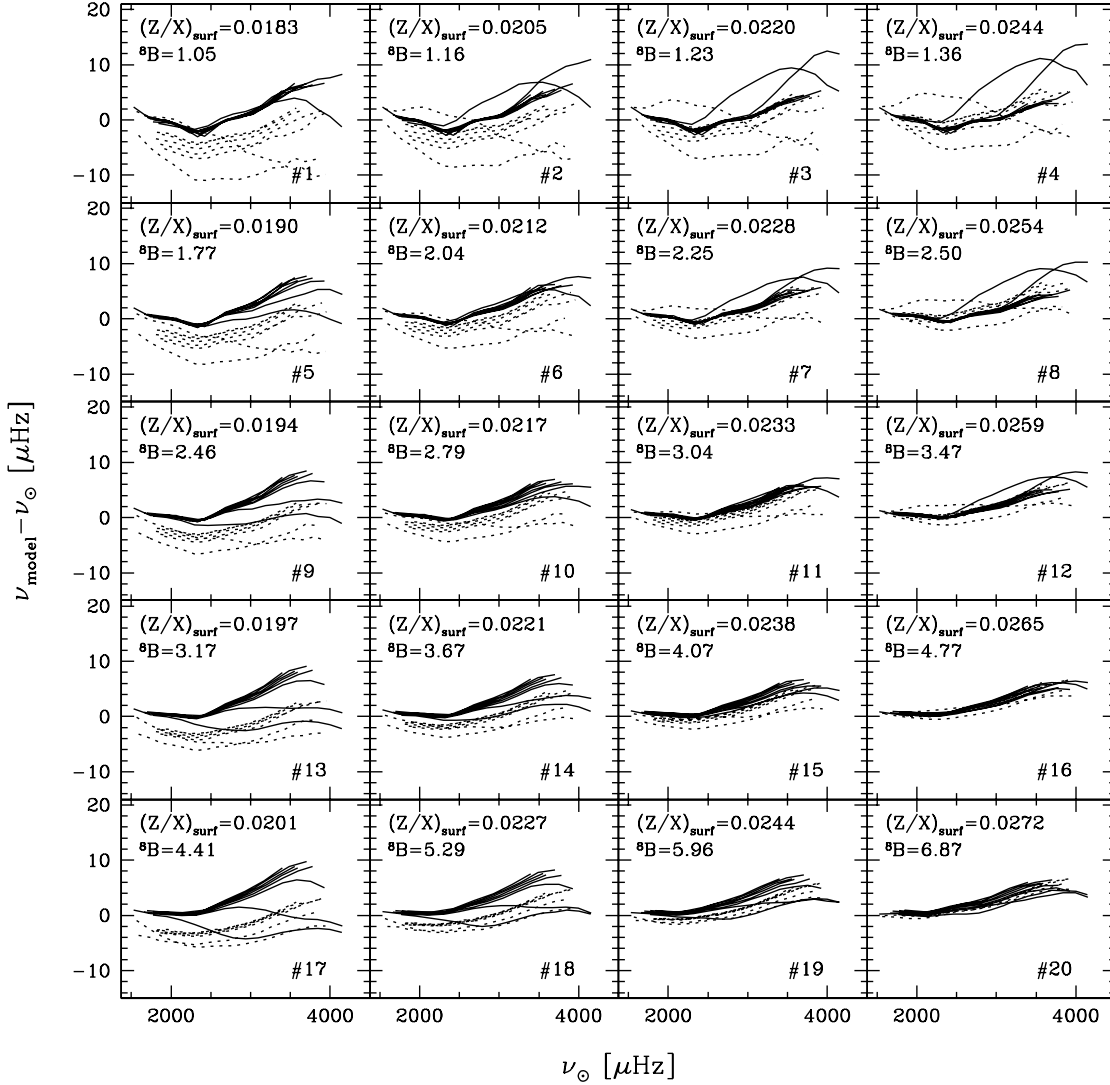


Fig. 1.— Grid of p -mode frequency difference plots, (model - Sun), for all models computed in this work. Lines connect data with a common l -value. Dashed lines correspond to $l=0, 4, 10$ and 20 . Solid lines correspond to $l=30, 40, 50, 60, 70, 80, 90$, and 100 . Each plot is annotated with the corresponding model number (see Tables 1-3), the surface Z/X ratio, and the ^8B neutrino flux, in $\text{cm}^{-2}\text{s}^{-1}$. Observational data used are from the MDI-SOHO data set (Rhodes et al. 1997).

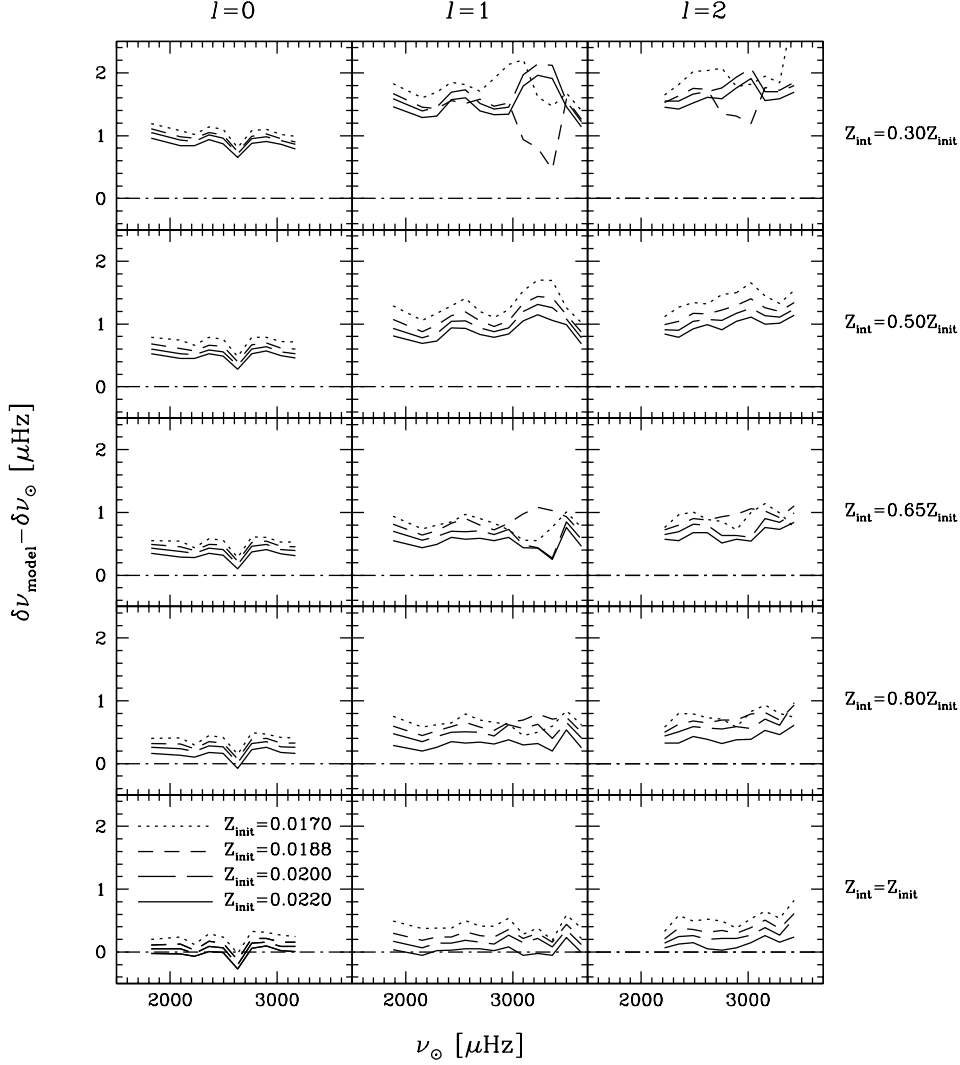


Fig. 2.— Grid of small spacing difference plots, (model - Sun), for all models computed in this work. Lines connect data from a particular model, indicated by Z_{int} and Z_{init} . Each row contains models of the same Z_{int} , where $Z_{\text{int}}=0.30Z_{\text{init}}$ includes models #1-4, $Z_{\text{int}}=0.50Z_{\text{init}}$ includes models #5-8, $Z_{\text{int}}=0.65Z_{\text{init}}$ includes models #9-12, $Z_{\text{int}}=0.80Z_{\text{init}}$ includes models #13-16, and $Z_{\text{int}}=Z_{\text{init}}$ includes the standard solar models #17-20. Each column contains results for a common l -value, with $l=0$ in column 1, $l=1$ in column 2, and $l=2$ in column 3. Observational data used are from the MDI-SOHO data set (Rhodes et al. 1997).

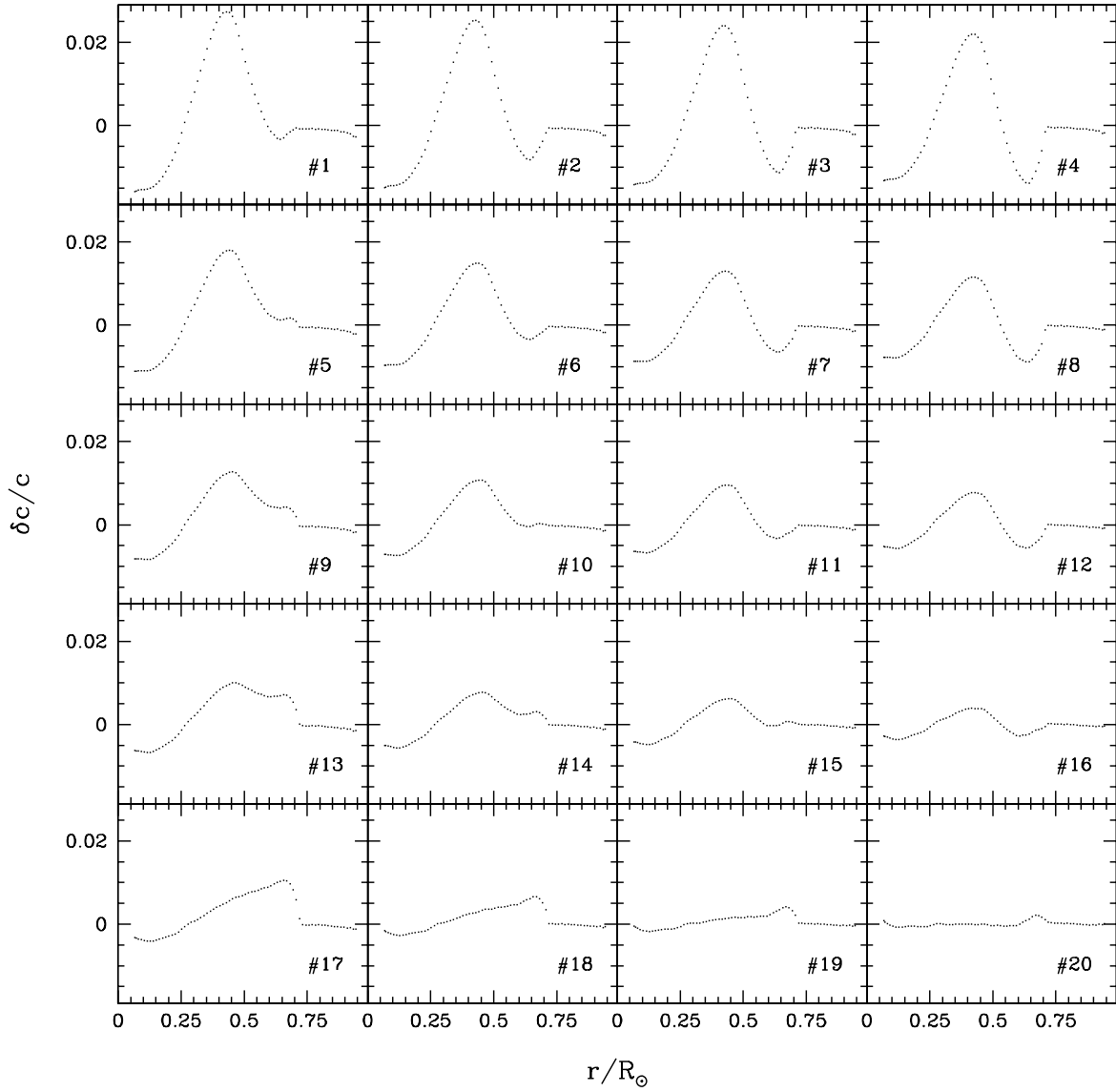


Fig. 3.— Grid of fractional difference plots for the sound-speed $((\text{Sun} - \text{model})/\text{model})$, for all models computed in this work. Solar sound-speed data were determined by Basu, Pinsonneault & Bahcall (2000) using the MDI-SOHO solar frequency data set (Rhodes et al. 1997).

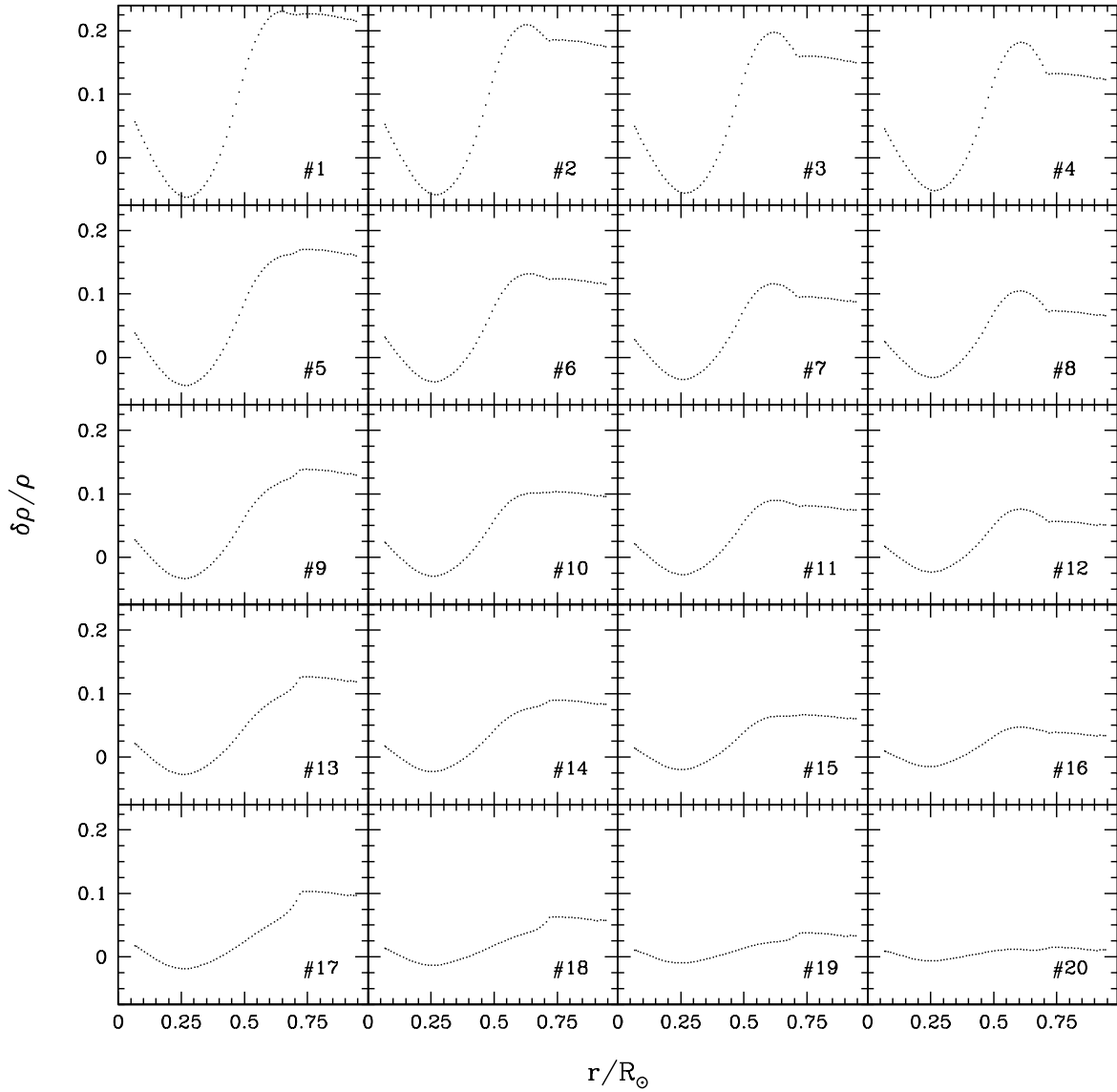


Fig. 4.— Grid of fractional difference plots for density ($(\text{Sun} - \text{model})/\text{model}$), for all models computed in this work. Solar density data were determined by Basu, Pinsonneault & Bahcall (2000) using the MDI-SOHO solar frequency data set (Rhodes et al. 1997).

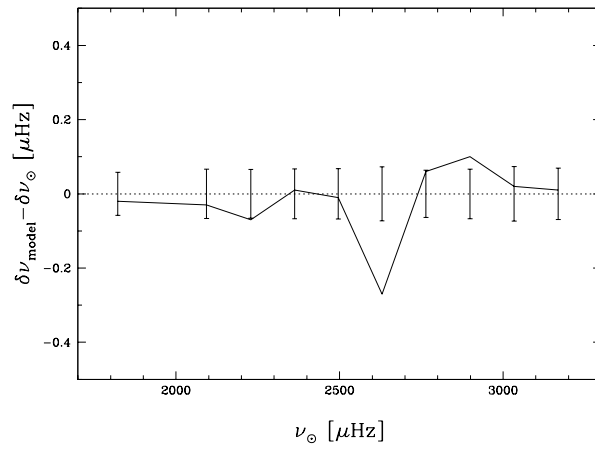


Fig. 5.— Small spacing difference plot (model - Sun), for standard solar model #20 with $l=0$. Observational data used are from the MDI-SOHO data set (Rhodes et al. 1997). The error bars plotted represent errors in the data. The observational uncertainties are approximately $\pm 0.07 \mu\text{Hz}$ for the small spacing determination.

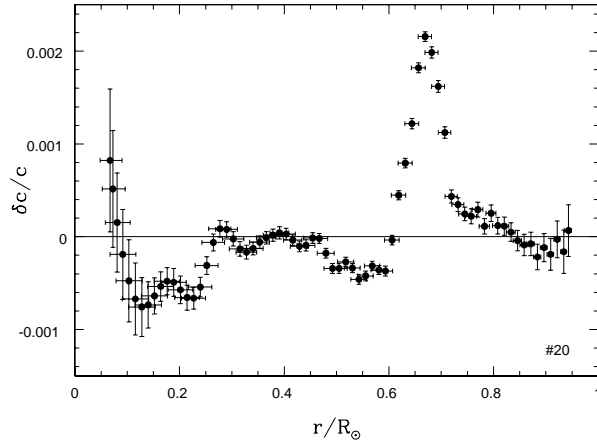


Fig. 6.— Fractional difference plot for the sound-speed $((\text{Sun} - \text{model})/\text{model})$, for standard solar model #20 (zoom in of Figure 3). Vertical error bars indicate 1σ errors in the inversion results due to errors in the data. Horizontal error bars are a measure of the resolution of the inversion.

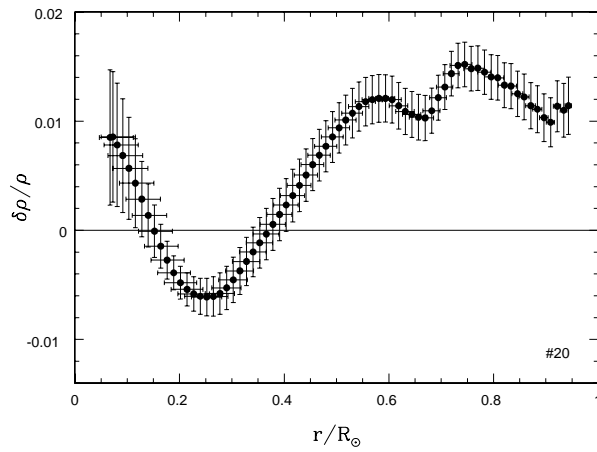


Fig. 7.— Fractional difference plot for density $((\text{Sun} - \text{model})/\text{model})$, for standard solar model #20 (zoom in of Figure 4).